Fermi National Accelerator Laboratory

FN-555
[E-687]

Photoproduction of D Mesons *

The E-687 Collaboration

presented by

D. Buchholz
Northwestern University
Evanston, Illinois 60208

October 1990

* Presented at the XXVth International Conference on High Energy Physics, Kent Ridge, Singapore, August 2-8, 1990.

Operated by Universities Research Association Inc. under contract with the United States Department of Energy

Photoproduction of D Mesons

P.L. Frabetti
Dip. di Fisica dell'Universita' and INFN - Bologna, I-40126 Bologna, Italy

C.W. Bogart, H. Cheung, P. Coteus,[a] S. Culy, J.P. Cumalat, D. Kaplan[b]
University of Colorado, Boulder, CO 80309, USA

J. Butler, F. Davenport,[c] I. Gaines, P. Garbincius, S. Gourlay, D. Harding, P. Kasper, A. Kreymer, P. Lebrun, H. Mendez,
Fermilab, Batavia, IL 60510, USA

S. Bianco, M. Enorini, F.L. Fabbri, A. Spallone, A. Zallo
Laboratori Nazionali di Frascati, I-00044 Frascati, Italy

R. Culbertson, M. Diesburg,[d] G. Jaross, K. Lingel, P. Sheldon, J.R. Wilson, J. Wiss
University of Illinois at Urbana-Champaign, Urbana, IL 61801, USA

G. Alimonti, G. Bellini, M. Di Corato, M. Giammarchi, P. Inzani, S. Malvezzi, P.F. Manfredi,[e] D. Menasce, E. Meroni, L. Moroni, D. Pedrini, L. Perasso, F. Ragusa, A. Sala, S. Sala, D. Torretta, M. Vittone[d]
Dip. di Fisica dell'Universita' and INFN - Milano, I-20133 Milan, Italy

D. Buchholz, C. Castoldi,[f] B. Gobbi, S. Park, R. Yoshida
Northwestern University, Evanston, IL 60208, USA

J.M. Bishop, J.K. Busenitz,[g] N.M. Cason, J.D. Cunningham, R.W. Gardner, C.J. Kennedy, E.J. Mannel, R.J. Mountain, D.L. Puseljic, R.C. Ruchti, W.D. Shephard, M.E. Zanabria
University of Notre Dame, Notre Dame, IN 46556, USA

G.L. Boca, R. Diaferia, S.P. Ratti, P. Vitulo
Dip. di Fisica dell'Universita' and INFN - Pavia, I-27100 Pavia, Italy

A. Lopez
University of Puerto Rico at Mayaguez, Puerto Rico

Presented by D. Buchholz for the Fermilab E687 Collaboration

[a]Present address: IBM TJ Watson Laboratories, Yorktown Heights, NY 10598
[b]Present address: University of Oklahoma, Norman, OK 73019, USA
[c]Present address: University of North Carolina, Ashville, NC 28804, USA
[d]Present address: Fermilab, Batavia, IL 60510, USA
[e]Present address: Dipartmento di Elettronica, Universita' di Pavia, Pavia, Italy
[f]Present address: Universita di Pavia and INFN, I-27100 Pavia, Italy
[g]Present address: University of Alabama, University, AL 35486, USA

Abstract

Preliminary results are presented using the Wide Band photon beam at Fermilab to measure the cross-section of $D^{*\pm}$ and $D^{\pm}$ photoproduction on a Be target over the photon energy range from 100 GeV to 350 GeV. Preliminary results are also presented on the x_F and p_T^2 distributions and the ratios of D^0/D^{*+} and D^{*-}/D^{*+}. The energy dependence of the total open charm cross-section of photoproduction was compared with the predictions by the photon-gluon fusion model and a higher order QCD radiative correction based on perturbative QCD. The prediction by the QCD radiative correction with $m_c \simeq 1.5$ GeV agrees well with the observed data within the theoretical uncertainties of the QCD parameters.

Introduction

Even though e^+e^- colliding beams have proven to be a reliable and clean way of producing charm particles, photoproduction experiments afford several advantages — the absolute production rates are orders of magnitude higher in photon beams because of much higher luminosity, and all portions of the charmed quark invariant mass spectrum can be observed simultaneously. Charm production has been also observed in hadroproduction but here the relative level of charm production is an order of magnitude lower than in photoproduction.

Recent advances and improvements in detector technology, especially, silicon strip detectors, enabled photoproduction and hadroproduction experiments to reduce their background substantially to the point at which final event samples were measured in the thousands and not tens. Experiment E687 of Fermilab is based on a new spectrometer with good vertex resolution provided by silicon strip detectors and powerful particle identification, and utilized the new Wide Band photon beam for a high statistics study of photoproduction and decays of charmed particles at the highest photon energies currently available. This paper presents a preliminary measurement of the photoproduction cross-section of $D^{*\pm}$ and $D^{\pm}$ extended into this new domain of photon energy. For the rest of this paper it will be assumed that D^{*+} and D^+ also refer to their charge conjugate states.

For the decay channel $D^{*+} \rightarrow D^0\pi^+$, the available rest mass energy $Q = M_{D^{*+}} - M_{D^0} - M_{\pi^+}$ is merely about 6 MeV. Since the Q is extremely small, in the lab frame the momenta of D^0 and the accompanying pion will be proportional to their masses. The low Q makes the resolution of the mass difference ΔM between D^{*+} and D^0 much higher than the resolution of the D^{*+} or D^0 mass alone because most of the measurement errors cancel during the subtraction. The resolution of ΔM is, typically, 1-2 MeV. In this analysis, D^{*+}'s have been identified exploiting the narrow ΔM peak as well as by finite lifetime tagging. D^+ and D^0 decays have been identified through lifetime tagging.

Detector

Experiment E687 was performed in the Fermilab Wide-Band Spectrometer [1] from June 1987 to February 1988. During this time approximately 60 million γ-nucleon triggers were recorded on tape. This paper presents preliminary results from this set.

The photon beam is created from 800 GeV protons which produce a tertiary 350 GeV electron beam which produces photons via bremsstrahlung. Due to the wide momentum acceptance of the beam the photon energies extend up to 400 GeV. The energy of the photon is measured from a knowledge of the incident energy and a measurement of the recoiling electron. The E687 photon beam is currently the world's highest energy accelerator photon beam.

The principal target used for the data taking was 5 segments of Be comprising about 11% of a radiation length. Silicon microstrip detectors were placed starting 6 cm downstream of the target. These were arranged in 4 stations each with three planes of microstrips. The transverse extrapolation of high momentum tracks found here is about 10 μm. In addition to these tracking planes charged particles were traced with five sets of four view multi-wire proportional chambers. The wire spacings were either 2 mm or 3 mm depending of where the chamber was located. There were two analysis magnets to provide the magnetic bend for momentum analysis. The bend was arranged in a vertical direction so that e^+e^- pairs were dispersed in a narrow vertical strip. This was used to advantage in the experiment trigger to avoid electromagnetic pair production. Neglecting multiple scattering which dominates below 20 GeV, the momentum of charged particles was measured with a resolution of about $\sigma/P = 1.4\% \times P/100GeV$ if they went through both analysis magnets and about $3.4\% \times P/100GeV$ if they only went through the first magnet. Three multi-cell gas threshold Čerenkov counters provided particle identification. The different gases used allowed K's to separated from π's and p's from, 5 to 60 GeV. Electrons and photons were measured in three electromagnetic calorimeters. An outer calorimeter measured the wide angle particles while the inner calorimeter measure those that went through both analysis magnets. Both of these calorimeters were lead scintillator devices. The very forward angle electromagnetic energy was measured in a lead lucite shower detector called the BGM. This was used principally to measure non-interacting photons. This detector was used to correct our knowledge of the interacting photon energy as well as serve as a luminosity monitor.

The hadron energy was measured in two hadron calorimeters arranged to catch the main hadrons going through both analysis magnets and also the very forward hadrons. The large calorimeter [2,3] consists of proportional tube chambers interspersed between planes of iron. The chambers are readout via induced signals in pads with a tower geometry. The very forward calorimeter was composed of sheets of uranium and scintillator. It is segmented only in two segments longitudinally.

Muons are detected in two areas, immediately behind the return yoke of the second analysis magnet and in the forward direction. Each detector consists of scintillator planes [4] and proportional tubes. The scintilators were used in a fast trigger while the tubes provide

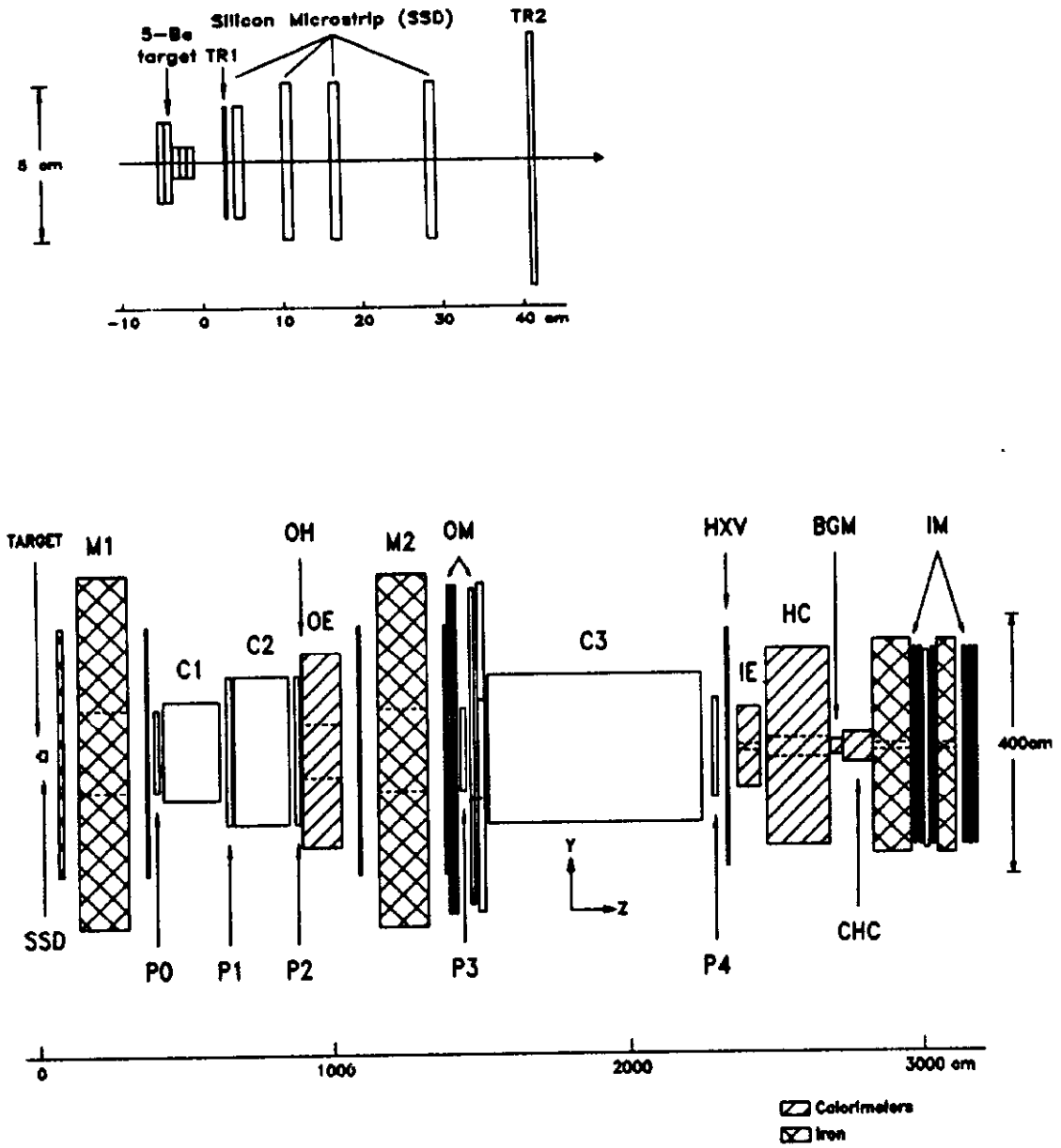

Figure 1: The layout of the E687 spectrometer.

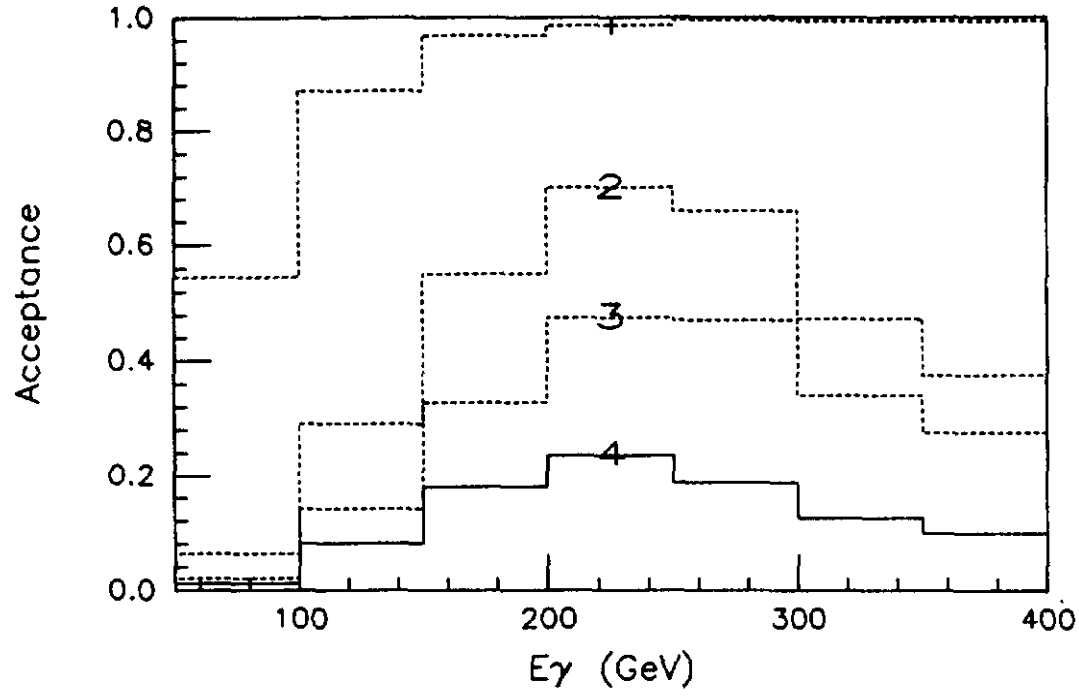

Figure 2: Acceptance of D^{*+} events. The acceptance curves as functions of the photon energy are for 1) after the master gate, 2) after the TRIGGER-1, 3) after the reconstruction, and 4) after all analysis procedures.

better position resolution.

A problem in locating charm particles is to develop a trigger that is restrictive enough so as not to be overwhelmed with data and yet not bias the data too much. The first level trigger used ensured that there was an interaction in the target and at least two particles further downstream in the apparatus. It also included a veto on charged particles in the beam and halo muons around the beam. A second level of triggering was more restrictive. This required that there be at least one set of hits in the first PWC plane outside of the expected pair region, that the recoil electron have an energy of less than about 200 GeV, and that there be at least 35 GeV of hadron energy observed in the hadron calorimeters. Figure 2 shows the effect of the trigger on the acceptance of D^{*+} events. The first curve shows the mild effect of the trigger counters. Curve 2 shows the effect of the PWC, hadron energy, and recoil electron requirement. Curve 3 shows the efficiency of the reconstruction and the final curve with an average efficiency of about 15% shows the effect of all the cuts and the final analysis.

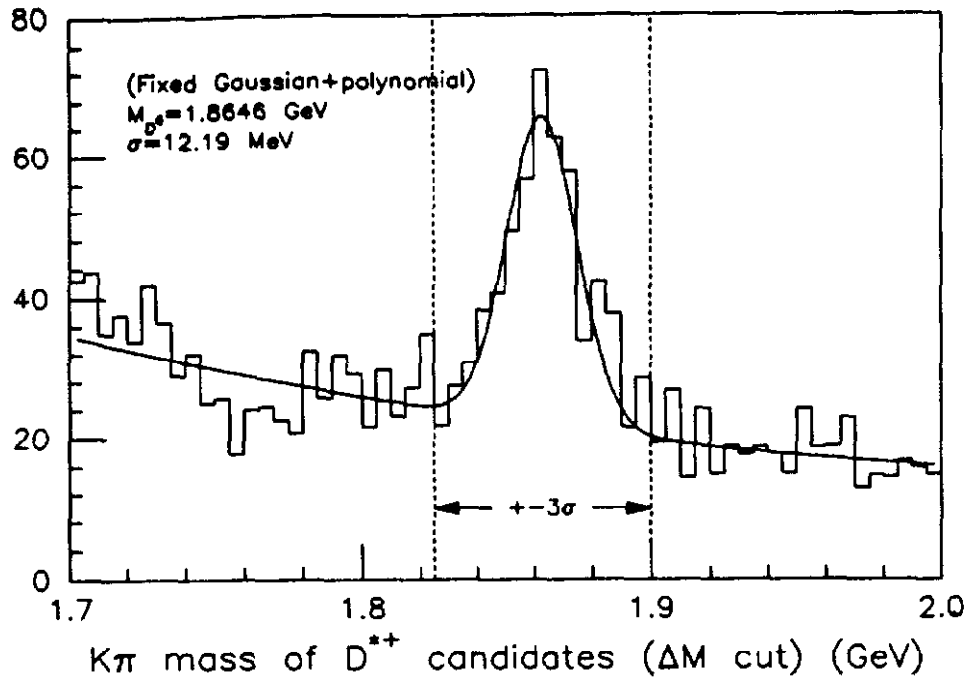

Figure 3: $M_{K\pi}$ of D^{*+} candidates after the cut $|\Delta M - 145.6\,\mathrm{MeV}| \leq 2.3\,\mathrm{MeV}$. The signal includes 293 ± 32 events.

Analysis

We begin by reporting two independent analyses of the D^{*+} photoproduction. The first approach relied heavily on the kinematics of the D^{*+} and used the clean decay channel $D^{*+} \to D^0\pi^+$; $D^0 \to K^-\pi^+$[5].

An alternate technique used both the ΔM cut and finite lifetime cuts. The lifetime tagging was accomplished with a candidate driven vertex algorithm [6]. In this algorithm the charm candidate tracks are fit to form a secondary vertex with a fit confidence level (DCL) and then formed into a track vector for the candidate. This track vector was then used as a seed for finding the primary vertex. Tracks are added to the primary vertex until a confidence level cut of 2% failed. A global fit is made to the candidate tracks which required the candidate to point back to the primary vertex taking correct account of all errors. The candidate tracks were choosen kinematically with a mild particle identification requirement.

These two D^{*+} analyses are complementary and allow us to check the consistency of the analysis. The kinematic technique which used a more restrictive set of the input data will be descibed first. Data was collected with several arrangements of the target. For the kinematic isolated analysis only data collected with a 5-segment beryllium target were used. There were 18 million triggers in this set. The D^{*+}'s are located by requiring the mass difference, ΔM, between the invariant mass of the $K\pi\pi$ combination and that of the $K\pi$ to

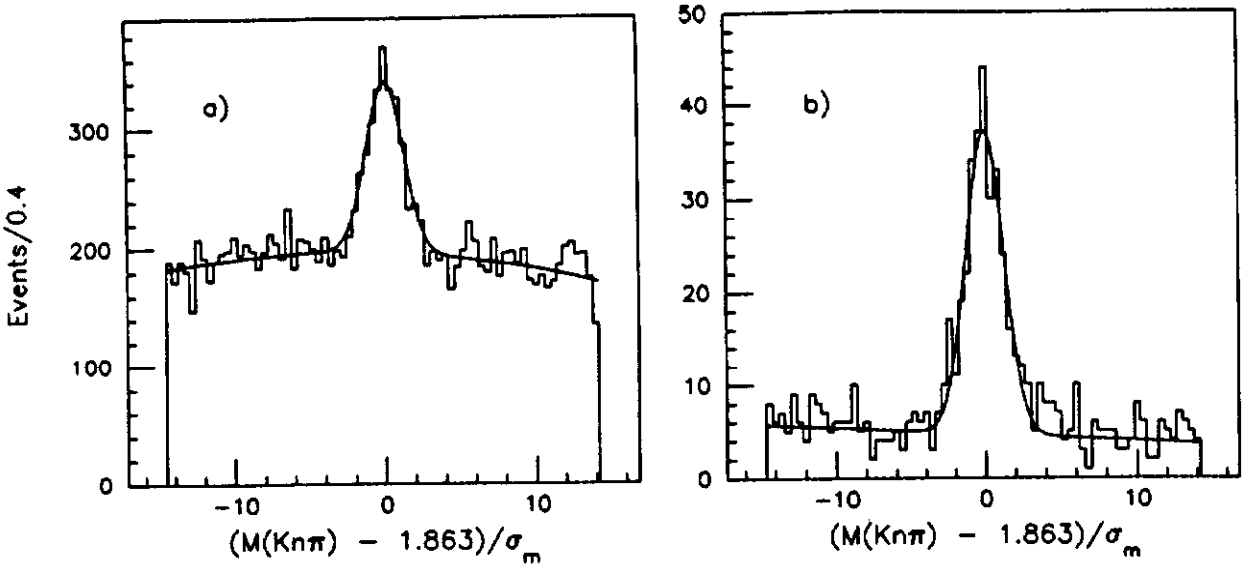

Figure 4: The observed mass less the nominal fitted mass divided by the error in the mass determination for a) for all D^0's from $D^0 \to K^-\pi^+\pi^+\pi^-$ and $D^0 \to K^-\pi^+$, and the same for b) for all D^0's from $D^{*+} \to D^0\pi^+$ followed by the same D^0 decays. There are 1135 ± 69 D^0 events in a) and 254 ± 18 D^0 events in b).

be $|\Delta M - 145.6\,\text{MeV}| < 2.3\,\text{MeV}$. The histogram in Figure 3 shows the invariant $K\pi$ mass of all D^{*+} candidates after this ΔM cut.

The curve in Figure 3 represents a Gaussian (1.8646 GeV, 12.19 MeV) with a second degree polynomial background. The parameters for the peak and the resolution of the D^0 mass in the E687 spectrometer were determined by fitting a relatively clean $M_{K\pi}$ sample selected using a candidate driven vertexing technique. The fit from this sample fits the data of figure 3 very well. The cross section for D^{*+} is determined from the data of Figure 3 after it is binned in photon energy ranges. The total number of D^{*+} from the histogram in Figure 3 is 293.0 ± 31.5 over a background of 348.1.

D^{*+} and D^0 have also been located using the candidate driven algorithm. In this case it is possible to obtain the $D^0 \to K^-\pi^+$ and $D^0 \to K^-\pi^+\pi^+\pi^-$ decay modes without the soft π trick used for the previous analysis. Figure 4 shows the sample of D^0 observed with this algorithm. The data sample used for this analysis is about 1/3 of the complete data. The figure shows the mass difference of either the $K\pi$ or $K3\pi$ less 1.863 GeV (the average observed mass) divided by the error in the mass determination. This sample gives 1135 ± 69 events from direct D^0 decays and 254 ± 18 events by the indirect D^{*+} to D^0 decay chain. This corresponds to 22 ± 9% of all D^0 are from the D^{*+} decay chain. This is consistent with a simple model that predicts that D^*'s and D's are produced in proportion to the number of spin states available (3:1) which predicts 0.29 ± 0.02 [7].

Using almost all of the data sample the D^{*+} decays are located with the candidate driven

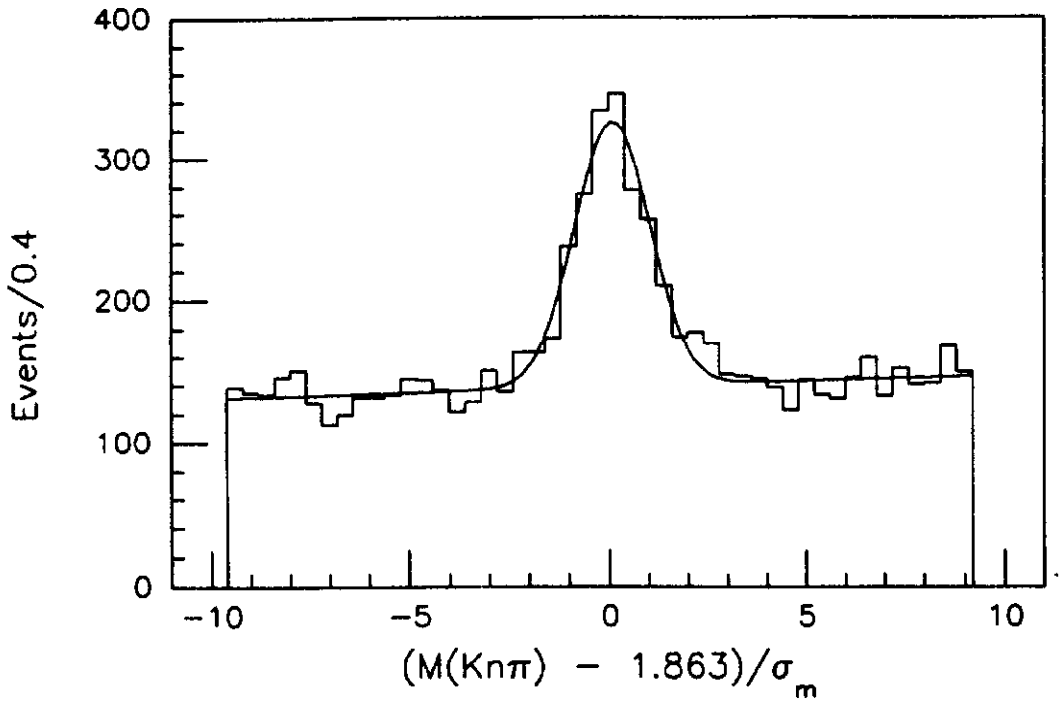

Figure 5: The mass difference of $K\pi$ and $K3\pi$ less the nominal mass over the error in the mass from from $D^{*\pm}$. There are 646 $\pm$ 35 events from $K\pi$ and 433 $\pm$ 35 events from $K3\pi$.

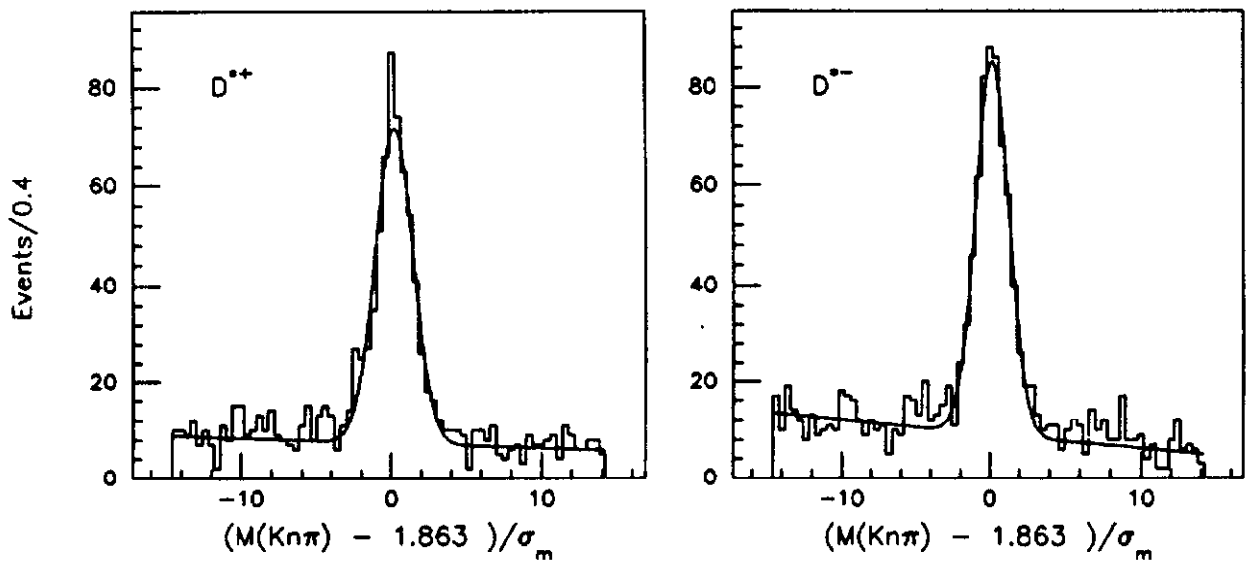

Figure 6: The $D^{*\pm}$ are separated into their respective charges. There are 509$\pm$ 26 events in the D^{*+} sample and 539$\pm$ 27 events in the D^{*-} sample.

algorithm and the mass plot is shown in Figure 5. There are 1109 ± 60 events in this sample. The same data sample can be split according to charge as orginating from D^{*+} or D^{*-} decays and is shown in figure 6. The ratio of antiparticle to particle is split evenly within statistics (1.06 ± 0.08) between the two charge states. This implies a low level of associated production of meson-baryon states at these energies. E691 [7] in the D^{*+} to D^0 decay found the value 1.15 ± 0.07 for $D^0 \to K^-\pi^+$and 1.23 ± 0.07 for $D^0 \to K^-\pi^+\pi^+\pi^-$.

To calculate the cross section we need the luminosity which is defined as

$$L \cdot \tau_{live} = \frac{N_\gamma \cdot N_A \cdot \rho_{Be} \cdot d_{eff}}{A_{Be}} \cdot \tau_{live} \tag{1}$$

where N_γ is the number of photons hitting the target, N_A is Avogadro's number, ρ_{Be} is the density of the Be target, A_{Be} is the atomic weight of Be, $d_{eff}(= 4.404 \times 0.5387\,\mathrm{cm})$ is the effective length of the Be target which is the Be target length multiplied by the targetting efficiency derived from a Monte Carlo, and τ_{live} is the live time of the data acquisition system (approximately 70 %). The number of photons was measured by an electromagnetic calorimeter, BGM. The BGM sees the sum of all forward electromagnetic energy (multiple photons, single photon, and e^+e^- pairs), and was scaled when the observed energy exceeded 133 GeV. To derive the actual number of photons from this scaled number, a simulation was done of the bremsstrahlung process in the radiator.

The acceptance of the E687 spectrometer and the efficiencies of the reconstruction and analysis program were estimated by simulating events with a complete set of Monte Carlo programs. The Monte Carlo simulated events were then processed by the same reconstruction and analysis programs as the actual data. The Monte Carlo programs for this study consisted of 3 parts — beam generation, event generation, and spectrometer simulation. For this experiment there were actually two independent Monte Carlo programs. This allows us to check the accuracy of each by comparison. We describe one of these for the D^{*+} decays, based on GEANT.

A photon beam Monte Carlo program generated photons by allowing electron passing through the lead radiator to radiate photons by the bremsstrahlung process. The electron beam energy spectrum was measured by the beam calorimeter, BGM, during a special calibration run for which the radiator and experimental target were removed and the analysis magnets were off. The photon beam Monte Carlo took account of the momentum spread in electron beam, the radiator thickness, and e^+e^- production within the radiator from a photon. Then the information on the photon energies and the attendant recoil electron was passed to the event generator.

The event generator simulates the photoproduction of charmed particles. The program was based on LUND Monte Carlo programs, LUCIFER 2.2, JETSET 6.3 and PYTHIA 4.8 [8,9,10]. For the LUCIFER Monte Carlo, the photon gluon fusion model (PGF) for photoproduction was chosen with a charm quark mass 1.6 GeV and a minimum momentum transfer in the photon-parton scattering of 0.2 GeV^2. For the gluon and quark structure functions in the PGF process, the EHLQ Set-1 structure functions with $Q^2 = 5\,\mathrm{GeV}^2$ [11]

were used. Then the quark dressing is done by the so-called "independent fragmentation"[9] with the Peterson function [12] with a coefficient of 0.18.

The event generator uses the photon energy from the beam generator program as input to the LUCIFER Monte Carlo to photoproduce charmed particles and spectator particles from the target nucleon fragmentation. In this analysis, only events including a D^{*+} from the charm quark were taken. There was no restriction on particle from the anti-charm quark as long as it included the anti-charm quark. This was done because we wanted to calculate the acceptance for inclusive charm production for all possible event topologies.

The spectrometer Monte Carlo program was based on GEANT 3.11 [13]. The geometry, materials, and efficiency information for all elements of the E687 spectrometer were put into the Monte Carlo program. The D^{*+}'s were always forced to decay via

$$D^{*+} \rightarrow D^0\pi^+;\ D^0 \rightarrow K^-\pi^+.$$

The anti-charm particles decayed according to the branching ratios listed by the Particle Data Group [14]. Then the spectrometer simulation of these particles was written in the same format as the real data on so-called "fake data" tapes. The fake data were analyzed by the same programs as were used for the real data analysis. The resultant D^{*+} mass plots were very similar to the experimentally observed ones.

The method to calculate a D^{*+} cross-section used in this analysis is derived from the following relation:

$$N(D^{*+} \rightarrow K\pi\pi) = B(D^{*+} \rightarrow K\pi\pi)\sigma(\gamma + Be \rightarrow D^{*+} + X) \cdot \epsilon \cdot L \cdot \tau_{live} \qquad (2)$$

where

N is the number of observed D^{*+} in the decay channel,

$L \cdot \tau_{live}$ is the luminosity times the live time (Eq. 1),

ϵ is the overall acceptance of the spectrometer and the reconstruction,

B is the branching ratio for the decay channel,

σ is the inclusive cross-section per Be nucleus.

Here

$$\begin{aligned} B(D^{*+} \rightarrow D^0\pi^+;\ D^0 \rightarrow K^-\pi^+) &= B(D^{*+} \rightarrow D^0\pi^+) \cdot B(D^0 \rightarrow K^-\pi^+) \\ &= (0.49 \pm 0.08) \times (0.0377 \pm 0.0037) \\ &= 0.0185 \pm 0.0035 \end{aligned}$$

from the Particle Data Group compilation [14]. Thus, the photon energy dependent cross-sections are calculated with the relation:

$$\sigma(\gamma + Be \rightarrow D^{*+} + X)(E_\gamma) = \frac{N(D^{*+} \rightarrow K\pi\pi)(E_\gamma)}{(0.0185 \pm 0.0035) \times 20.54 \times f(E_\gamma) \times \epsilon(E_\gamma)}\ \text{nb} \qquad (3)$$

where the argument E_γ indicates the parameter is energy dependent.

Results

For the D^{*+} cross-section energy dependence, the D^{*+} signals were partitioned in 50 GeV bins from 100 to 350 GeV and the signals were determined from the invariant mass histograms. Using Eq. 2 and Eq. 3, the D^{*+} inclusive photoproduction cross-sections for the photon energy range from 100 GeV to 350 GeV were calculated.

Table 1: Inclusive D^{*+} photoproduction cross-section.

Photon energy[a] (GeV)	Average energy[b] (GeV)	Number of $D^{*\pm}$	Cross-section[c] (μb)
100–150	140	75.03 ± 14.22	$5.88 \pm 1.16 \pm 1.57$
150–200	175	77.46 ± 13.67	$4.31 \pm 0.78 \pm 1.15$
200–250	209	71.32 ± 16.03	$4.15 \pm 0.95 \pm 1.10$
250–300	261	42.60 ± 13.50	$4.29 \pm 1.38 \pm 1.14$
300–350	292	24.64 ± 6.772	$6.72 \pm 1.94 \pm 2.64$

[a]Measured by tagging system.

[b]Corrected average value explained in the text.

[c]The first error is statistical and the second is systematic.

The results are listed in Table 1. The cross-section is the sum of D^{*+} and D^{*-} cross-sections on a Be nucleus and the errors listed include statistical and systematic errors. The systematic error was estimated from uncertainties in the branching ratios, luminosity calculations, trigger efficiencies, particle identification, data analysis, and photon energy calculations to be 26.6% . The acceptance is corrected for the entire x_F range. The resultant energy dependence of the cross-section is shown in Figure 7. When events are reconstructed the incident photon energy is measured with considerable uncertainty, mostly due to a lack of knowledge of the incident electron beam momentum($\pm 45\,GeV$). The relation between the measured and actual photon energy is modeled with a Monte Carlo. The resultant cross section represents a weighted average of the "actual" cross section with a gaussian weighting function. The horizontal bars in Figure 7 represent the σ of the gaussian weighting function.

Table 2: Inclusive D^{*+} photoproduction cross-section with $x_F > 0.2$. The D^{*+} are identified with the candidate driven algorithm for this sample.

Photon energy (GeV)	Central energy (GeV)	$D^{*\pm}$ Cross-section[a] (μb)
85–165	125	$3.07 \pm 0.48 \pm 0.82$
165–250	207.5	$4.08 \pm 0.60 \pm 1.09$
250–350	300	$3.80 \pm 0.92 \pm 1.01$

[a]The first error is statistical and the second is systematic .

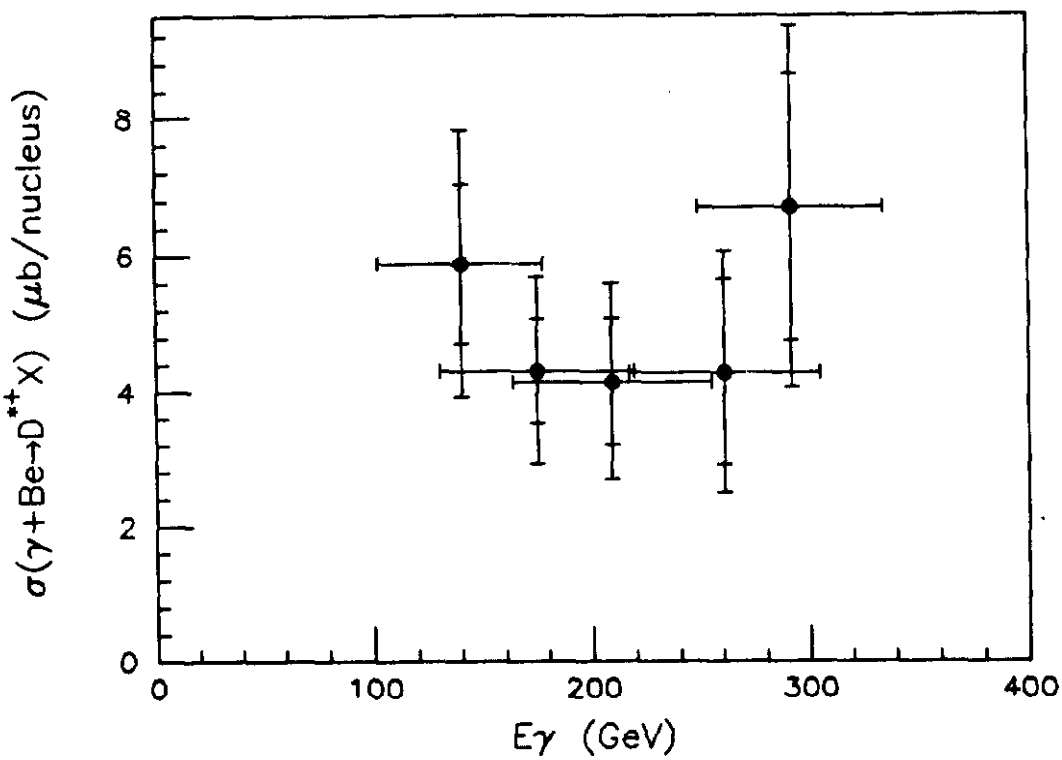

Figure 7: The E_γ dependence of the cross-section on Be for D^{*+}. The inner error is statistical, and the outer error includes the systematic error in quadrature.

The results for the candidate driven algorithm search for D^{*+} are listed in Table 2 and are shown in Figure 8 . This sample is based on 927 ± 39 events and includes $D^0 \rightarrow K^-\pi^+\pi^+\pi^-$ decays in addition to the $D^0 \rightarrow K^-\pi^+$ which the previous sample was based on. The branching ratio of $D^0 \rightarrow K^-\pi^+\pi^+\pi^-$ is taken as 0.0790. In this alternative analysis, an attempt is made to correct for the large uncertainty in the incident photon energy ($\approx \pm 45\ GeV$) by de-convoluting the cross section in measured x_F and E_γ bins with the expected energy resolution as determined by Monte Carlo simulation. The basic approach [15] is to use the Monte Carlo to construct a matrix $R_{i\alpha}$ which relates the number of observed events within the i'th bin of measured x_F and E_γ (n_i) to the partial cross sections ($\Delta\sigma_\alpha$) used to generate the events where the α index refers to a bin of true x_f and E_γ.

$$n_i = \sum_\alpha R_{i\alpha}\ \Delta\sigma_\alpha \tag{4}$$

By using sufficiently small bins, the dependence of $R_{i\alpha}$ on the production model used in the Monte Carlo can be minimized.

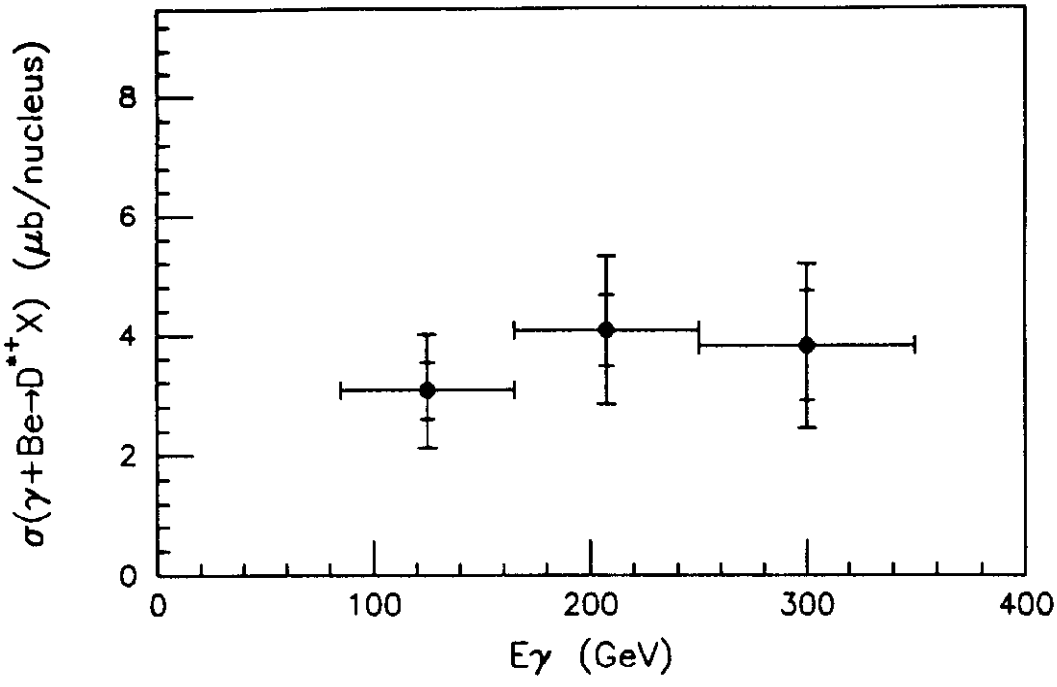

Figure 8: The E_γ dependence of the cross-section on Be for $D^{*+} \to D^0\pi^+$; $D^0 \to K^-\pi^+$ and $D^{*+} \to D^0\pi^+$; $D^0 \to K^-\pi^+\pi^+\pi^-$ with $x_F > 0.2$. The inner error is statistical only, and the outer error includes the systematic error in quadrature.

Eq. 4 is solved using a weighting technique. Each charm candidate is assigned a weight based on its measured x_F and E_γ value and the Monte Carlo generated $R_{i\alpha}$ matrix. The area under the signal peak in the weighted mass histogram serves to measure the cross section, the error in the signal area reflects the statistical, de-convolution, as well as background subtraction errors. The horizontal error bars in figure 8 represent the width of the energy bin. The data are restricted to the region $x_F > 0.2$.

Table 3: Inclusive $D^\pm$ photoproduction cross-section with $x_F > 0$.

Photon energy (GeV)	Central energy (GeV)	$D^\pm$ Cross-section[a] (μb)
100–181	141.5	$3.07 \pm 0.43 \pm 0.82$
181–264	222.5	$4.66 \pm 0.93 \pm 1.24$
264–347	305.5	$5.58 \pm 1.59 \pm 1.48$

[a]The first error is statistical and the second is systematic .

The results for the search for the $D^+ \to K^-\pi^+\pi^+$ decay via the candidate driven algorithm requiring a detachment of the primary and secondary vertices in excess of five standard

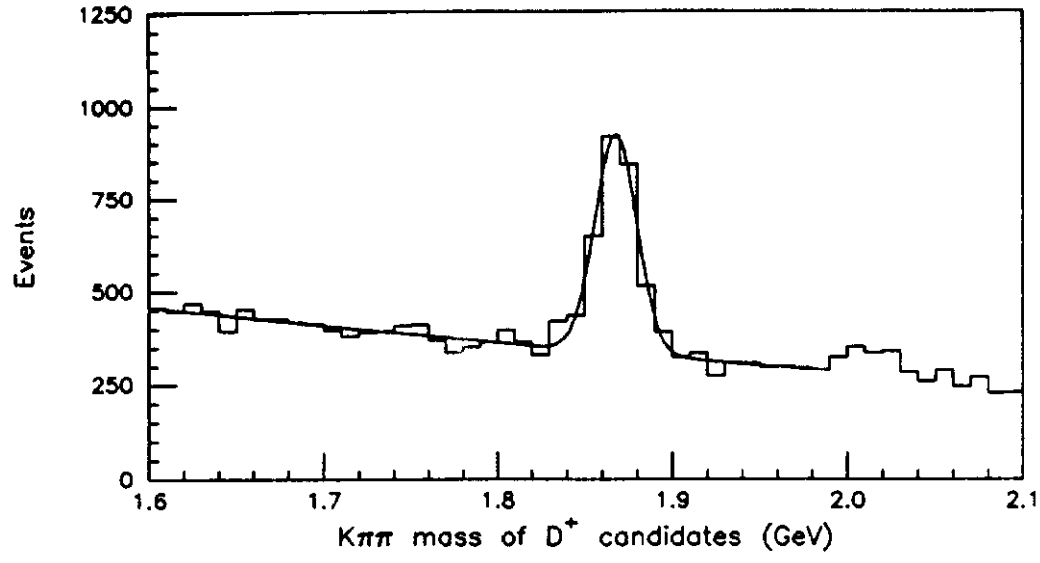

Figure 9: The $M_{K\pi\pi}$ of D^+ candidates. The plot includes 1757 ± 70 events and the fitted mass is $1.8680 \pm 0.0012\,GeV$.

deviations are shown as a mass plot in Figure 9. The cross section obtained with the de-convolution are listed in Table 3 and are shown in Figure 10 [15]. This cross section is based on the branching ratio of $D^+ \to K^-\pi^+\pi^+$ of 0.078. The horizontal error bars in Figure 10 represent the width of the energy bin as in previous figure.

The p_T^2 dependence of the cross-section with the acceptance correction was calculated and the resultant differential cross-section $d\sigma/dp_T^2$ for D^{*+} and D^+ is shown in Figure 11 and is fitted by the empirical form

$$d\sigma/dp_T^2 \propto \exp(-bp_T^2 + cp_T^4), \tag{5}$$

with $b = 1.14 \pm 0.23$ (0.92 ± 0.05) and $c = 0.098 \pm 0.045$ (0.036 ± 0.007) for the $D^{*+}(D^+)$. The average p_T^2 for $D^{*+}(D^+)$ derived from the differential cross-section data is

$$\langle p_T^2 \rangle = 1.33 \pm 0.68(1.26 \pm 0.19)\,\mathrm{GeV}^2/c^2$$

which is consistent with the value $1.27 \pm 0.13\,\mathrm{GeV}^2/c^2$ for D^{*+} and $1.21 \pm 0.06\,\mathrm{GeV}^2/c^2$ for D^+ observed by E691 [7].

The x_F distribution via the de-convolution method for the D^{*+} events is shown in Figure 12 along with the same distribution for D^+. The curve superimposed is not a fit but rather a representative curve with the parametrization as given by E691 [7].

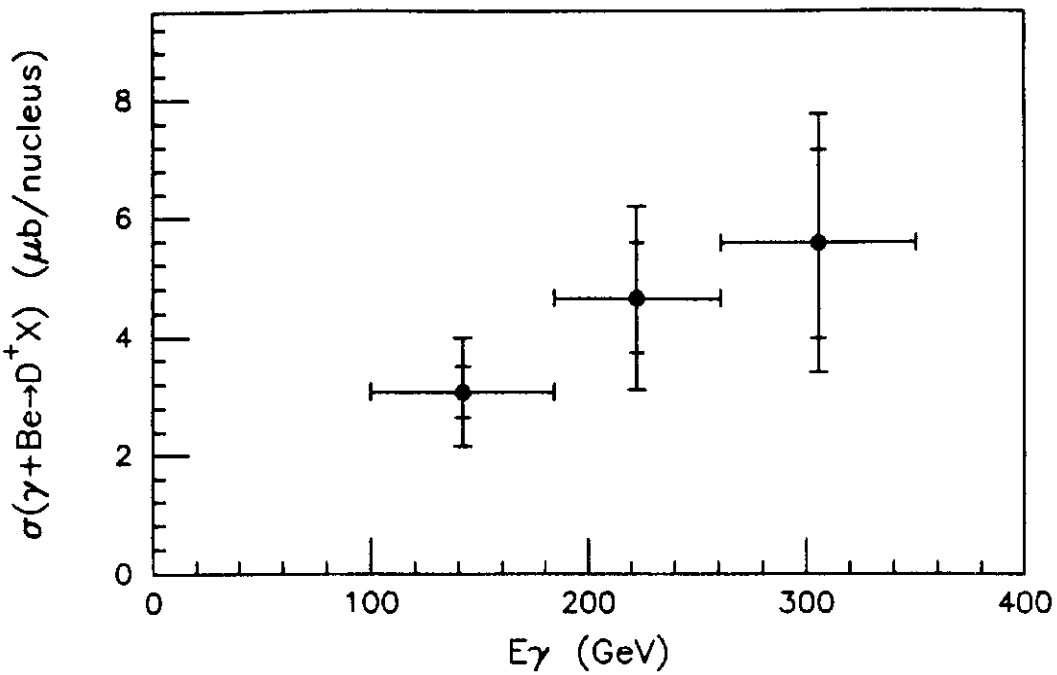

Figure 10: The E_γ dependence of the cross-section on Be for $D^+ \rightarrow K^-\pi^+\pi^+$ with $x_F > 0$. The inner error is statistical, and the outer error includes the systematic error in quadrature.

Total Open Charm Photoproduction Cross-section

The photon-gluon fusion model (PGF) [16] is the interpretation of photoproduction based on the lowest order process of perturbative QCD. In this process, the photon couples to a heavy quark anti-quark pair and then one of the quarks is scattered by a gluon from the target. The process is closely related to the calculable Bethe-Heitler quantum electrodynamics (QED) process.

The total open charm photoproduction cross-section can be derived from the D^{*+} cross-section obtained in this analysis. The fraction of D^{*+} among all open charm particles produced in the photoproduction process is only dependent on the charm quark fragmentation after the $c\bar{c}$ pair is created. The LUND Monte Carlo program [8,9] was used to calculate the ratio of D^{*+} to all open charm particles from $c\bar{c}$. The "string fragmentation" was chosen since it properly took account of the kinematic correlations of the pair of charmed particles. The resultant ratios of charmed particles are listed in Table 4. The rate in the table is the probability that a charmed particle or its charge conjugate is produced from a $c\bar{c}$ event. The rate for the D^{*+} is derived to be 0.604. For the A dependence of the cross-section, we assumed that A^α with $\alpha = 0.93$ following E691's choice [7]. We assume that the uncertainty of the rate simulation of the rate and the choice of A dependence contribute an additional systematic error of 5%, e.g. replacing the string fragmentation model with the independent

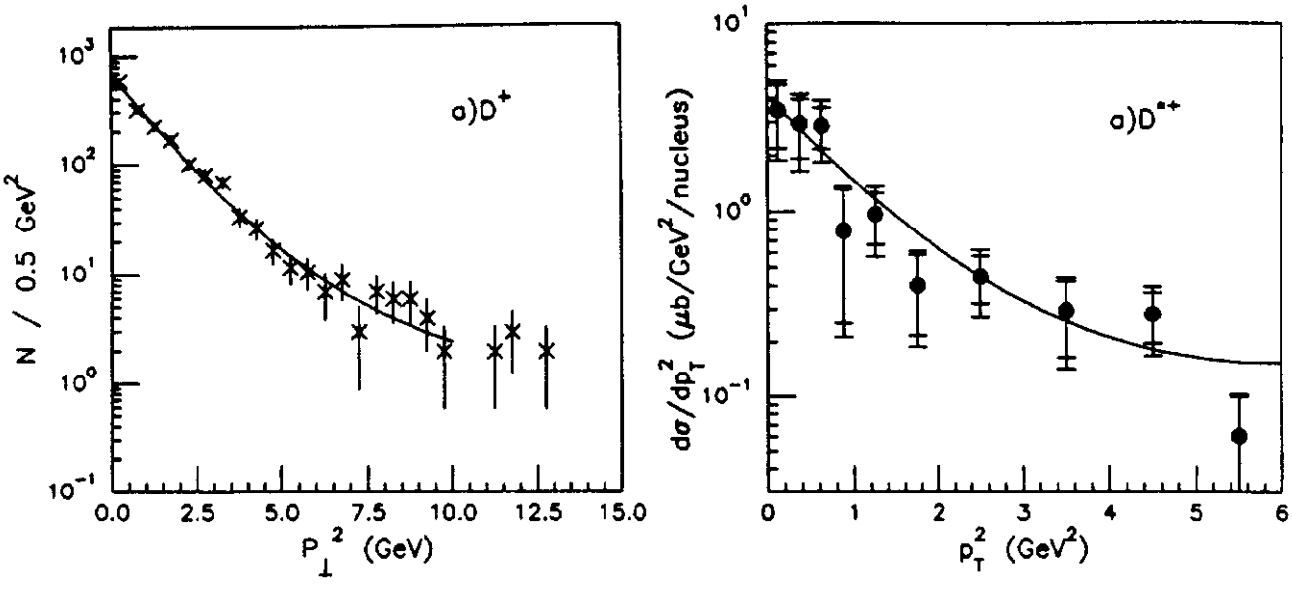

Figure 11: The p_T^2 dependence of the cross-section on Be for a) D^+ and b) D^{*+}. The inner error is statistical, and the outer error also includes the systematic error in quadrature. The fitted curve is described in the text.

fragmentation model lowers the D^{*+} fraction by 3%. This calculation leads to the total open charm photoproduction cross-section per nucleon of:

$$\sigma_{c\bar{c}}/\text{nucleon} = \frac{\sigma_{D^{*+}}/\text{Be}}{0.604 \times 9.01^{0.93}}$$

The data of Table 2 can also be used to calculate the total open charm cross-section but it must be further corrected for the limited x_F range. The E691 parameterization [7] predicts that 55% of all x_F will have $x_f > 0.2$. When the data of Table 3 is used, it is corrected by assuming that $x_F > 0$ is 89% of all the x_F acceptance. The $D^{\pm}$ is corrected by the string fragmentation of Table 4 by $0.203 + 0.604 \times 0.51 = 51\%$. The 0.51 is the branching fraction of D^{*+} into D^+. The energy dependence of the total open charm cross-section calculated from these three tables is shown in Figure 13. Figure 13 also shows the published data from other experiments on open charm photoproduction. These data are from the compilation given in Ref. [23] and from the NA14′ [24] and E691 [7] papers. For E691 data, the data of the photon energy dependence of the cross-section in the article [7] were multiplied by the factor $1/A^{0.93} = 0.129$ to convert the cross-section from per Be nucleus to per nucleon.

Several parameters must be chosen to compare these results with the photon gluon fusion model prediction. The charm quark mass m_c, the QCD scale parameter Λ, the momentum transfer Q^2, and the gluon distribution $G(x)$ are required. A prediction from the PGF model

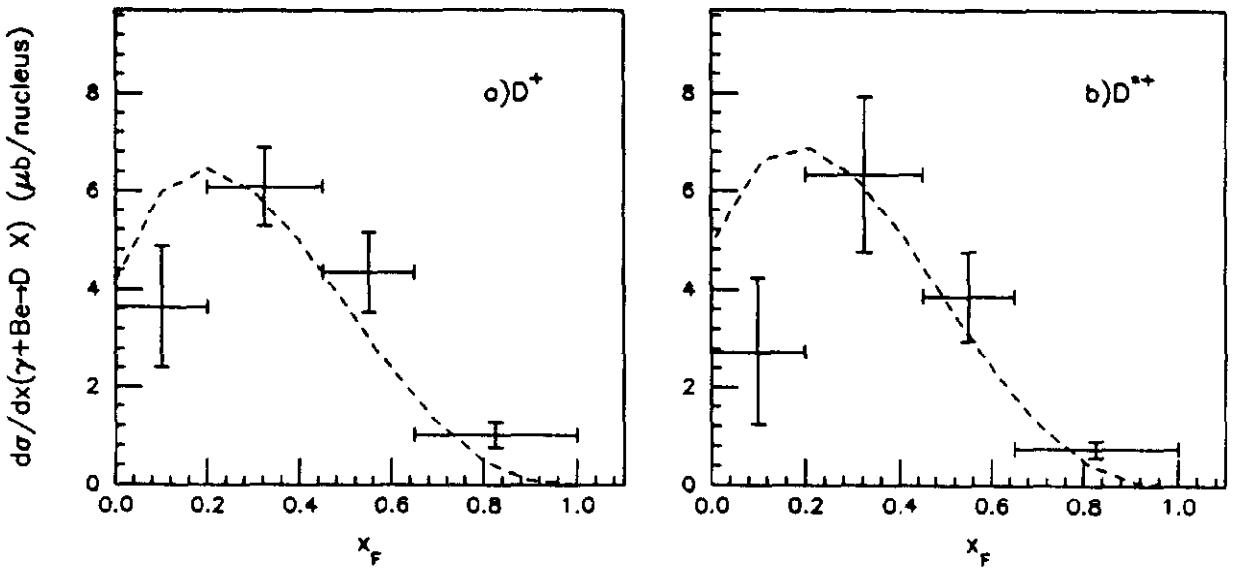

Figure 12: The x_F dependence of the cross-section on Be for a) $D^{\pm}$ and b) D^{*+}. The error is statistical only. The curve is described in the text.

with the naive gluon distribution using the QCD parameters $Q^2 = 10\,\mathrm{GeV}^2$ and $\Lambda = 260\,\mathrm{MeV}$ did not give a good comparison with data.

The higher order QCD radiative correction model was thought to give more realistic predictions. Figure 14 shows the estimation of the cross-section using QCD radiative correction [17]. The QCD parameters selected were $Q^2 = 10\,\mathrm{GeV}^2$ and $\Lambda = 260 \pm 100\,\mathrm{MeV}$. The gluon distribution used is a naive one. The m_c's used are 1.2 GeV, 1.5 GeV, and 1.8 GeV. In each plot, the solid curve is for the choice in $\Lambda = 260\,\mathrm{MeV}$ and $Q^2 = 10\,\mathrm{GeV}^2$, and the dotted curves are corresponding to the uncertainties of Λ of $\pm 100\,\mathrm{MeV}$, and Q of a factor of two. In the QCD radiative correction model, smaller value of m_c ($= 1.2\,\mathrm{GeV}$) are not consistent

Table 4: The ratio of charm particles to $c\bar{c}$ events by LUND.

Charmed particle and its c.c.	Rate per $c\bar{c}$ by String Fragmentation
D^0	0.212
D^+	0.203
D_s^+	0.057
D^{*0}	0.620
D^{*+}	0.604
D_s^{*+}	0.165
Charmed baryons $J = 1/2$	0.102
Charmed baryons $J = 3/2$	0.038

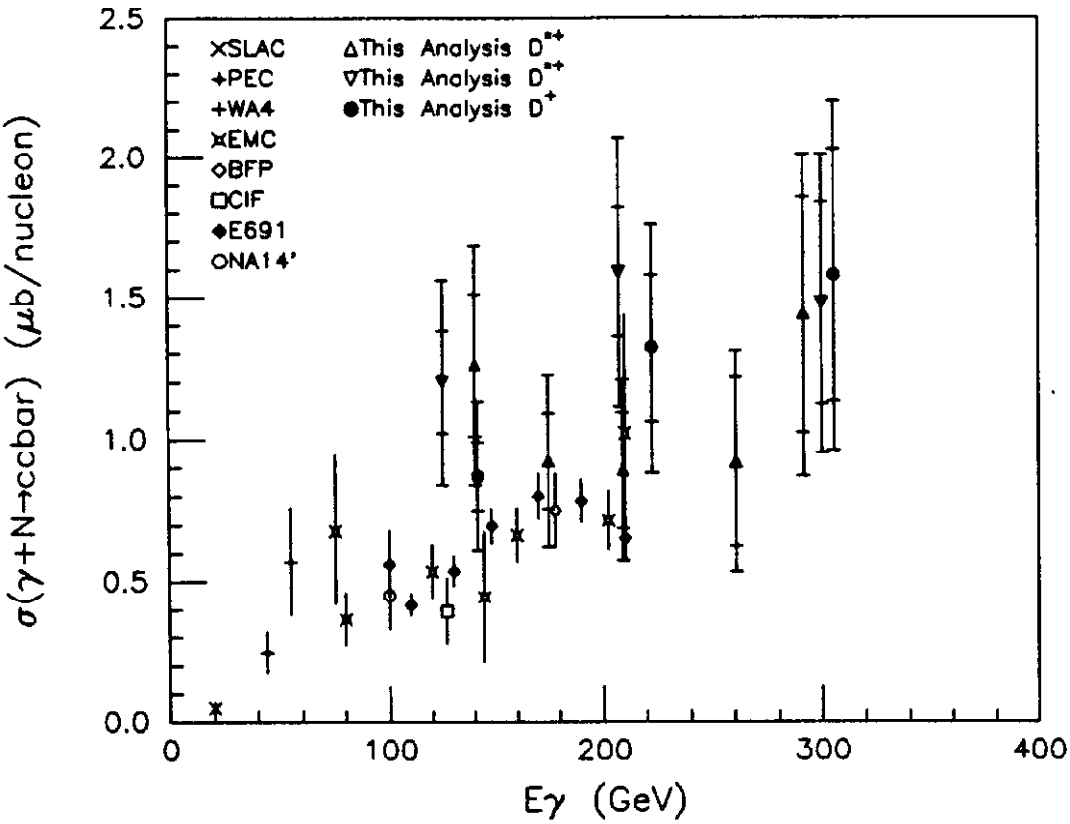

Figure 13: The photon energy dependence of the total cross-section per nucleon for photoproduction of open charm events. The data points with Δ are derived from the D^{*+} with the kinematic analysis, ∇ are derived from the D^{*+} with the lifetime analysis, and $\bullet$ are derived from the D^{+} from this analysis. For these the inner error is statistical, and the outer error includes the systematic error in quadrature. The data points for other experiments come from CIF [18], BFP [19], WA4 [20], SLAC [21], EMC [22], PEC [23], E691 [7], and NA14′ [24].

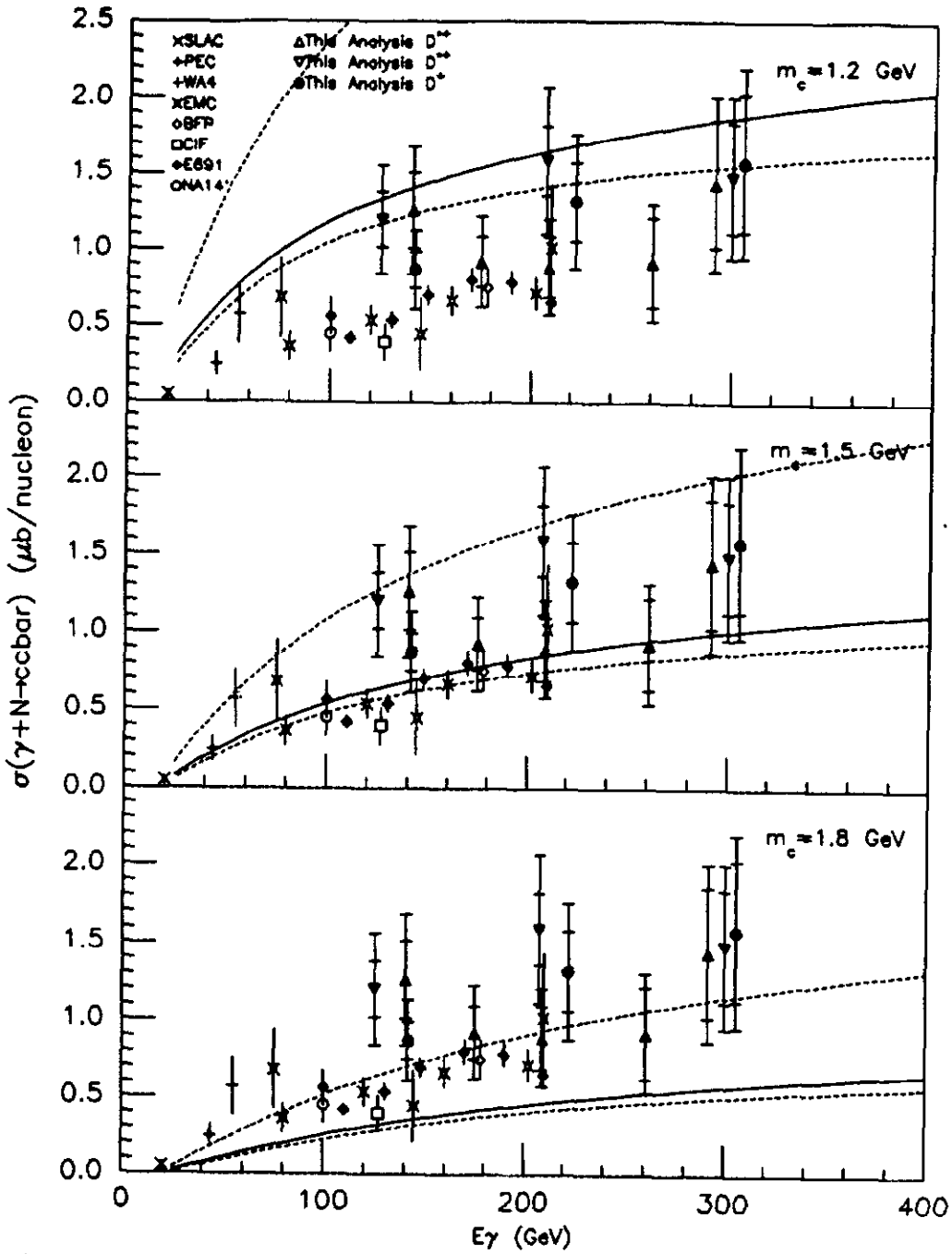

Figure 14: The total charm photoproduction cross-section by QCD radiative correction [17]. Data points are the same as Figure 13. The three plots from top are for m_c =1.2, 1.5, 1.8 GeV, respectively. The solid curves are for Λ = 260 MeV, and the dotted curves are for the uncertainties of Λ and Q^2.

with the data. The total cross-section of open charm photoproduction presented here are in reasonable agreement with the other data and the prediction with $m_c = 1.5\,\mathrm{GeV}$.

Conclusions

We have extended the range of photoproduction of $D^{*\pm}$ and $D^{\pm}$ to the world's highest energy. The energy dependence of the $D^{*\pm}$ and $D^{\pm}$ inclusive photoproduction cross-section is given up to 350 GeV. The total charm cross-sections derived from the $D^{*\pm}$ and $D^{\pm}$ cross-sections are consistent with the data from other experiments within the errors. The prediction of the charm photoproduction cross-section by the QCD radiative correction by Ellis et al. [17] is consistent with the observed data when using reasonable QCD parameters. Within the available statistics, the observed p_T^2 and x_F distributions and $\langle p_T^2 \rangle$ are consistent with other experiments.

Acknowledgements

We wish to acknowledge the assistance of the staffs of Fermilab, INFN of Italy and the physics departments of the University of Colorado, University of Illinois, Northwestern University, and University of Notre Dame. This research was supported in part by the National Science Foundation, the U.S. department of Energy, the Italian Istituto Nazionale di Fisica Nucleare and Ministero della Universita' e della Ricerca Scientifica.

References

[1] "Description of the E687 spectrometer", submitted to this conference by S. Gourlay for the Fermilab E687 Collaboration.

[2] S. Park et al., "Hadron Calorimeter with Proportional Tubes and Pad Readout", IEEE Transactions On Nuclear Science, Vol. 35, No. 1, 516, (1987).

[3] S. Park et al., "Performance of the Hadron Calorimeter for FNAL Experiment E687", Nucl. Inst. and Methods, A289, 496, (1990).

[4] R. Yoshida et al., "Tetrode Photmultiplier Base for High Magnetic Field Environments", IEEE Transactions On Nuclear Science, Vol. 33, No. 1, (1986).

[5] S. Park, Ph.D. Thesis, Northwestern University, unpublished (1990).

[6] "D^+, D^0 Signals and Lifetimes in E687 Photoproduction Experiment at Fermilab ", submitted to this conference by L. Moroni for the Fermilab E687 Collaboration.

[7] J.C. Anjos et al., Phys. Rev. Lett. 62 (1989) 513.

[8] G. Ingelman and A. Weigend, "LUCIFER — A Monte Carlo for High-$p_\perp$ Photoproduction," Comput. Phys. Commun. 46 (1987) 241.

[9] T. Sjöstrand and M. Bengtsson, "The Lund Monte Carlo for Jet Fragmentation and e^+e^- Physics - JETSET version 6.3," Comput. Phys. Commun. 39 (1986) 347.

[10] H.-U. Bengtsson and T. Sjöstrand, "The Lund Monte Carlo for Hadronic Processes - PYTHIA version 4.8," Comput. Phys. Commun. 46 (1987) 43.

[11] E. Eichten et al., "Supercollider Physics," Rev. Mod. Phys. 56 (1984) 579.

[12] C. Peterson et al., Phys. Rev. D27 (1983) 105.

[13] R. Brun et al., "GEANT3," CERN Data Handling Division DD/EE/84-1, 1987.

[14] Particle Data Group, "Review of Particle Properties," Phys. Lett. B204 (1988).

[15] K. Lingel, Ph.D. Thesis, University of Illinois, unpublished (1990).

[16] L.M. Jones and H.W. Wyld, Phys. Rev. D17 (1978) 759.

[17] R.K. Ellis and P. Nason, Nucl. Phys. B312 (1989) 551.

[18] M.S. Atiya et al., CIF Collab., Phys. Rev. Lett. 43 (1979) 414.

[19] A.R. Clark et al., BFP Collab., Phys. Rev. Lett. 45 (1980) 682.

[20] D. Aston et al., WA4 Collab., Phys. Lett. B94 (1980) 113.

[21] K. Abe et al., Phys. Rev. Lett. 51 (1983) 156.

[22] J.J. Aubert et al., EMC Collab., Nucl. Phys. B213 (1983) 31; Phys. Lett. B167 (1986) 127.

[23] M.I. Adamovich et al., Photon Emulsion Collab., Phys. Lett. B187 (1987) 437.

[24] M.P. Alvarez et al., The NA14′ Collab., CERN-EP/88-148 (Oct. 1988).